Available online at www.sciencedirect.com
ScienceDirect
Journal of Computational Physics 226 (2007) 1645–1667
JOURNAL OF COMPUTATIONAL PHYSICS
www.elsevier.com/locate/jcp

A global finite-difference semi-Lagrangian model for the adiabatic primitive equations

Saulo R.M. Barros *, Claudia I. Garcia

Instituto de Matemática e Estatística, Universidade de São Paulo, R. do Matão 1010, 05508-090 São Paulo, Brazil

Received 3 August 2006; received in revised form 24 May 2007; accepted 7 June 2007
Available online 22 June 2007

Abstract

We develop a global semi-implicit semi-Lagrangian model for the atmospheric adiabatic primitive equations discretized through finite-differences. The model formulation includes a new semi-Lagrangian treatment of the continuity equation and a spatially averaged Eulerian handling of the orography. These techniques contribute to the accuracy and efficiency of the scheme. The semi-Lagrangian discretization makes the integration method very stable; we can carry out integrations with time-steps which by far exceed the CFL time-step limitations of Eulerian schemes. We carry out several numerical experiments, showing that good accuracy is achieved even when we triple the time-steps. Our numerical experiments also demonstrate the computational efficiency of the method; we can run 10 days simulations at fine resolutions in a few hours on a personal computer.
© 2007 Elsevier Inc. All rights reserved.

PACS: 92.60.Wc; 02.70.Bf; 02.60.Cb; Ams 65M06

Keywords: Semi-Lagrangian; Finite-differences; Global weather models; Primitive equations; Multigrid

1. Introduction

Semi-Lagrangian methods have been widely adopted in global numerical weather prediction models, in conjunction with spectral [17,19], finite-elements [7] and finite-differences [6,12,10] discretizations. The main advantage of semi-Lagrangian schemes is the fact that they are not limited by CFL-type restrictions in the choice of time-step sizes, leading, in principle, to computationally more efficient schemes. There are, however, several aspects to be considered in the development of an efficient numerical method for the global primitive equations.

In the present article, we develop a three-time-level semi-implicit semi-Lagrangian method, based on a finite-difference discretization, for the three-dimensional primitive equations. We employ a uniform latitude–longitude Arakawa C-grid on the sphere and a pressure based σ vertical coordinate. The semi-Lagrangian scheme is formulated in vector form and is handled as in [16]. We introduce a new

* Corresponding author. Tel.: +55 11 30916136; fax: +55 11 30196131.
E-mail addresses: saulo@ime.usp.br (S.R.M. Barros), claudiag@ime.usp.br (C.I. Garcia).

0021-9991/$ - see front matter © 2007 Elsevier Inc. All rights reserved.
doi:10.1016/j.jcp.2007.06.011

semi-Lagrangian treatment of the continuity equation, employing a mean (vertically averaged) wind in the advection of surface pressure. The treatment of this equation becomes essentially two-dimensional and therefore cheaper than other approaches as in [6] or [17]. We compare our formulation with those other approaches and get similar accuracy in the numerical experiments at lower computational costs. We have also adapted the spatially averaged Eulerian treatment of orography proposed in [18] to our finite-difference model. Our experiments show the advantages of this formulation in the presence of steep orography, especially if large time-steps are employed.

For the validation of the model we have employed the test case suggested by Polvani et al. [13]. We have run several tests, at different resolutions, and we have obtained good agreement with the results given in [13].

We present numerical results demonstrating the stability of the scheme, even with time-steps which exceed by far the CFL constraints of Eulerian schemes. At every time-step of the model, the semi-implicit part of the discretization leads to a three-dimensional scalar equation to be solved. This equation is decomposed into a set of two-dimensional Helmholtz-type equations, through the use of the precomputed eigenvectors of the matrix of the vertical structure. We show that this is possible and that the resulting equations are elliptic, by proving that the vertical structure matrix has a complete set of eigenvectors and that all its eigenvalues are positive. The Helmholtz-type equations are solved efficiently with the help of a multigrid solver adapted from [2]. The computational complexity of the scheme varies linearly with an increase in the number of grid-points in each model layer, in contrast with a higher complexity of spectral methods which employ Legendre transforms. Only the process of decoupling the three-dimensional scalar equation associated with the semi-implicit discretization has a higher complexity, being quadratic on the number of layers of the model. The final efficiency of the model is very good. We are able to carry out 10 days forecasts at a spatial resolution of less than one degree (0.9375°), with 28 vertical layers, in about three and half hours on a personal computer (with a 3.2 GHz Pentium 4, 2 MB cache and 3 GB of memory).

The paper is arranged as follows. In Section 2, we present the complete description of the model. A series of numerical experiments focusing on the model validation, the multigrid performance, the variations of treatment of the orography and of the continuity equation, the use of large time-steps and its effect on accuracy and results on the model performance are presented in Section 3. We finish with some conclusions. We also point out that the present work is a step towards a variable resolution model for the primitive equations, in continuation to our work with shallow-water models [4].

2. The model formulation

The dry, adiabatic, primitive equations build the core of most global weather models. They are given by the momentum equations

$$\frac{\mathrm{d}\mathbf{V}}{\mathrm{d}t} + f\mathbf{k}\times\mathbf{V} + \nabla_{\mathrm{H}}\Phi + RT\nabla_{\mathrm{H}}\ln p_{\mathrm{s}} = 0, \tag{1}$$

the thermodynamic equation

$$\frac{\mathrm{d}T}{\mathrm{d}t} = \frac{\kappa T}{\sigma p_{\mathrm{s}}}\omega = \kappa T\left(\frac{\dot{\sigma}}{\sigma} + \frac{\partial \ln p_{\mathrm{s}}}{\partial t} + \mathbf{V}\cdot\nabla_{\mathrm{H}}\ln p_{\mathrm{s}}\right) \tag{2}$$

and the continuity equation

$$\frac{\partial \ln p_{\mathrm{s}}}{\partial t} + \mathbf{V}\cdot\nabla_{\mathrm{H}}\ln p_{\mathrm{s}} + D + \frac{\partial\dot{\sigma}}{\partial\sigma} = 0, \tag{3}$$

where we have adopted $\sigma = p/p_{\mathrm{s}}$ as the vertical independent coordinate (p is pressure and p_{s} it's value on the Earth's surface). The 'horizontal' coordinates are latitude and longitude (λ,θ), covering the whole sphere. The prognostic variables of the model are the horizontal wind field $\mathbf{V} = (u,v)$, the temperature T and the surface pressure p_{s}. The other variables in the equations, which can be obtained diagnostically, are the geopotential height Φ, obeying the hydrostatic equation:

$$\sigma\frac{\partial\Phi}{\partial\sigma} + RT = 0 \tag{4}$$

and the pressure vertical velocity $\omega = \mathrm{d}p/\mathrm{d}t$. The Coriolis factor is $f = 2\Omega\sin\theta$, R is the gas constant, $\kappa = R/c_\mathrm{p}$ and c_p is the specific heat at constant pressure. ∇_H is the horizontal gradient on a σ surface ($\nabla_\mathrm{H} = \frac{\mathbf{i}}{a\cos\theta}\frac{\partial}{\partial\lambda} + \frac{\mathbf{j}}{a}\frac{\partial}{\partial\theta}$) and $D = \nabla_\mathrm{H}$. $\mathbf{V}$ is the horizontal divergence. The total derivative is given by:

$$\frac{\mathrm{d}}{\mathrm{d}t} = \frac{\partial}{\partial t} + \mathbf{V}\cdot\nabla_\mathrm{H} + \dot{\sigma}\frac{\partial}{\partial\sigma} \tag{5}$$

where $\dot{\sigma} = \mathrm{d}\sigma/\mathrm{d}t$ is the vertical velocity. The coordinate σ varies from 1 at the surface of the Earth to 0 at the top of the atmosphere. As boundary conditions we have $\dot{\sigma} = 0$ for $\sigma = 0$ and $\sigma = 1$. The computational domain is given by $\{(\lambda,\theta,\sigma) \in [-\pi,\pi]\times[-\pi/2,\pi/2]\times[0,1]\}$.

2.1. Time discretization

We employ a three-time-level semi-implicit semi-Lagrangian temporal discretization of the equations. The basic idea is to split each equation for a field F as

$$\frac{\mathrm{d}F}{\mathrm{d}t} + N + L = 0, \tag{6}$$

where L is a linear (or linearized) part of the equation to be treated implicitly and N contains the non-linear terms to be handled explicitly. Eq. (6) is discretized as

$$\frac{F^{n+1} - F^{n-1}_*}{2\Delta t} + N^n_M + \overline{L^n} = 0, \tag{7}$$

where we introduce the notation:

$$N^n_M := \frac{N^n + N^n_*}{2}, \quad \overline{L^n} := \frac{L^{n+1} + L^{n-1}_*}{2}.$$

Superscripts refer to time instants, for instance, F^n means field F at time $t_n = t_0 + n\Delta t$. The integration is carried out along a Lagrangian trajectory. For each computational grid-point, where we will compute a new value F^{n+1}, there is a corresponding departure point (denoted by the $*$ subscript) at time t_{n-1}, such that a fluid particle will evolve from the $*$ point till the corresponding grid-point in a time-interval of $2\Delta t$. The departure points are computed (as in [16]) through the iterative scheme

$$r^{(k+1)} = \beta^{(k)}(g - \Delta t\mathbf{V}(r^{(k)}, \sigma^{(k+1)}, t)) \tag{8}$$

with

$$\sigma^{(k+1)} = \sigma - \Delta t\dot{\sigma}(r^{(k)}, \sigma^{(k)}, t), \tag{9}$$

where g is the computational grid-point at a σ model layer. The superscripts denote the iteration number, with $(r^{(k)}, \sigma^{(k)}) = (\lambda^{(k)}_r, \theta^{(k)}_r, \sigma^{(k)})$ being the approximation to the mid-point of the trajectory. Following [14] the approximation to $r^{(k+1)}$ in Eq. (8) is done on a tangent plane to the spherical surface on a σ-layer, and projected into this surface (through the multiplication by $\beta^{(k)}$). In this iterative process the values of the horizontal and vertical velocities need to be interpolated to the approximation locations, since those do not in general coincide with grid-points. For this purpose we employ bilinear interpolation. Once the mid-point of the trajectory is computed (two iterations are normally sufficient), the departure points are determined by symmetric (with respect to the mid-point) extension of the computed trajectory. This extension is done along a great circle on the sphere, and linearly in σ. In case any computed departure point lies below the first vertical layer or above the last we nudge it to the closest layer.

We notice that the non-linear terms in (7) are approximately evaluated at the middle of the Lagrangian trajectory at time t_n, as the average of their values at the locations of the computational grid-point and of the corresponding departure point. The linear terms at time t_{n-1} are evaluated at the same departure points. For the computations at departure points we employ a quasi-cubic interpolation. This is a modification of a tri-cubic interpolation, which reduces the 64 points stencil to a 32 points stencil (see [8]).

We now give a more detailed description of the time discretization of the primitive equations. The momentum equations are discretized as

$$\frac{\mathbf{V}^{n+1}-\mathbf{V}_*^{n-1}}{2\Delta t}+\overline{(f\mathbf{k}\times\mathbf{V})^n}+(RT'\nabla_{\mathrm{H}}\ln p_{\mathrm{s}})_M^n+\overline{\nabla_{\mathrm{H}}P^n}=0, \tag{10}$$

where the temperature is split as $T=T_0+T'$, with T_0 constant (we take $T_0=300$ K) and the generalized geopotential is defined as $P=\Phi+RT_0\ln p_{\mathrm{s}}$ (with the two-dimensional field $\ln p_{\mathrm{s}}$ being added to Φ at every level σ).[1]

For the discretization of the thermodynamic equation we need an expression for $\dot{\sigma}$. We integrate the continuity equation (3) in order to get:

$$-\frac{\partial\ln p_{\mathrm{s}}}{\partial t}=\int_0^1(\mathbf{V}\cdot\nabla_{\mathrm{H}}\ln p_{\mathrm{s}}+D)\mathrm{d}\sigma \tag{11}$$

and

$$\begin{aligned}\dot{\sigma}&=(1-\sigma)\frac{\partial\ln p_{\mathrm{s}}}{\partial t}+\int_\sigma^1(\mathbf{V}\cdot\nabla_{\mathrm{H}}\ln p_{\mathrm{s}}+D)\mathrm{d}\sigma\\&=-(1-\sigma)\int_0^1(\mathbf{V}\cdot\nabla_{\mathrm{H}}\ln p_{\mathrm{s}}+D)\mathrm{d}\sigma+\int_\sigma^1(\mathbf{V}\cdot\nabla_{\mathrm{H}}\ln p_{\mathrm{s}}+D)\mathrm{d}\sigma.\end{aligned} \tag{12}$$

Expressions (11) and (12) are used in the discretization of the thermodynamic equation:

$$\begin{aligned}\frac{T^{n+1}-T_*^{n-1}}{2\Delta t}=&\left(\kappa T\left(\mathbf{V}\cdot\nabla_{\mathrm{H}}\ln p_{\mathrm{s}}-\int_0^1(\mathbf{V}\cdot\nabla_{\mathrm{H}}\ln p_{\mathrm{s}})\mathrm{d}\sigma\right)\right)_M^n+\left(\kappa T'\left(\frac{\dot{\sigma}}{\sigma}-\int_0^1 D\,\mathrm{d}\sigma\right)\right)_M^n\\&-\overline{\left(\kappa T_0\int_0^1 D\,\mathrm{d}\sigma\right)^n}+\frac{\kappa T_0}{\sigma}\left(-(1-\sigma)\int_0^1\mathbf{V}\cdot\nabla_{\mathrm{H}}\ln p_{\mathrm{s}}\,\mathrm{d}\sigma+\int_\sigma^1\mathbf{V}\cdot\nabla_{\mathrm{H}}\ln p_{\mathrm{s}}\,\mathrm{d}\sigma\right)_M^n\\&+\frac{\kappa T_0}{\sigma}\overline{\left(-(1-\sigma)\int_0^1 D\,\mathrm{d}\sigma+\int_\sigma^1 D\,\mathrm{d}\sigma\right)^n}.\end{aligned} \tag{13}$$

For the semi-Lagrangian treatment of the continuity equation (11) we define the mean wind $\bar{\mathbf{V}}=\int_0^1\mathbf{V}\,\mathrm{d}\sigma$ and introduce the two-dimensional total derivative

$$\left(\frac{\mathrm{d}}{\mathrm{d}t}\right)_2=\frac{\partial}{\partial t}+\bar{\mathbf{V}}\cdot\nabla_{\mathrm{H}} \tag{14}$$

to get the expression

$$\left(\frac{\mathrm{d}}{\mathrm{d}t}\right)_2\ln p_{\mathrm{s}}+\int_0^1 D\,\mathrm{d}\sigma=0, \tag{15}$$

which is discretized as

$$\frac{\ln p_{\mathrm{s}}^{n+1}-\ln p_{\mathrm{s}}^{n-1}{}_{*_2}}{2\Delta t}+\frac{\int_0^1 D^{n+1}\,\mathrm{d}\sigma+(\int_0^1 D^{n-1}\,\mathrm{d}\sigma)_{*_2}}{2}=0. \tag{16}$$

The departure points $*_2$ are obtained from the two-dimensional mean-wind trajectory.

It has been observed that semi-Lagrangian schemes may present spurious resonant responses to orographic forcing [11,18]. A modification has been proposed by Ritchie and Tanguay [18] for a spectral model, which makes this problem much less severe. We adapt their suggestion, introducing a variation for the discretization of the continuity equation. For this, consider the splitting:

[1] We also considered the explicit treatment of the Coriolis terms as an option in the code. Results were in general similar, but in some cases a bit noisier. We have chosen the implicit handling of the Coriolis terms as our primary option. This may be more relevant for two-time-level models (see for example [19]), which we consider in our future developments.

$$\ln p_s = l' - \frac{\Phi_s}{RT_0}, \tag{17}$$

where Φ_s is the geopotential orography (gravity times the height of the Earth's topography). With this definition, the field l' will be much smoother than $\ln p_s$, which varies strongly with the bottom topography. We write then the continuity Eq. (15) as an equation for l' and discretize it in the form

$$\frac{l'^{n+1} - l'^{n-1}_{*_2}}{2\Delta t} + \frac{\int_0^1 D^{n+1}\,\mathrm{d}\sigma + (\int_0^1 D^{n-1}\mathrm{d}\sigma)_{*_2}}{2} - \left(\frac{\bar{\mathbf{V}}\cdot\nabla_H\Phi_s}{RT_0}\right)^n_M = 0. \tag{18}$$

In our numerical experiments we compare both approaches, presenting evidence of the benefits of this modification. Also other variations in the way the continuity equation is treated in global models [6,17], will be considered.

2.2. Vertical discretization

Our vertical discretization is based on CPTEC's model, which originated from COLA's GCM [9], with the introduction of necessary modifications for a semi-Lagrangian formulation. The atmosphere is divided into N_σ layers, where layer k has width Δ_k. The layers are numbered 1 to N_σ, from the Earth's surface to the top of the atmosphere (actually following the variable $\hat{\sigma} = 1 - \sigma$, with $\Delta_k = \hat{\sigma}_{k+1} - \hat{\sigma}_k$), as shown in Fig. 1. Each model variable is represented at the middle of each layer, with the exception of the vertical velocity, which is stored at layer interfaces. Also the surface pressure and the geopotential orography are only defined at the Earth's surface. The vertical integrals are approximated (with second order accuracy) by the repeated application of the mid-point rule.

In order to complete the discretization, we still need a way of evaluating the geopotential Φ, which is part of the generalized geopotential P used in Eq. (10). For this we make use of two forms of the hydrostatic equation. First we integrate (4) (using that $\sigma\partial\Phi/\partial\sigma = \partial/\partial\sigma(\sigma\Phi) - \Phi$) in order to get

$$\int_0^1 \Phi\,\mathrm{d}\sigma = \Phi_s + \int_0^1 RT\,\mathrm{d}\sigma, \tag{19}$$

discretized as

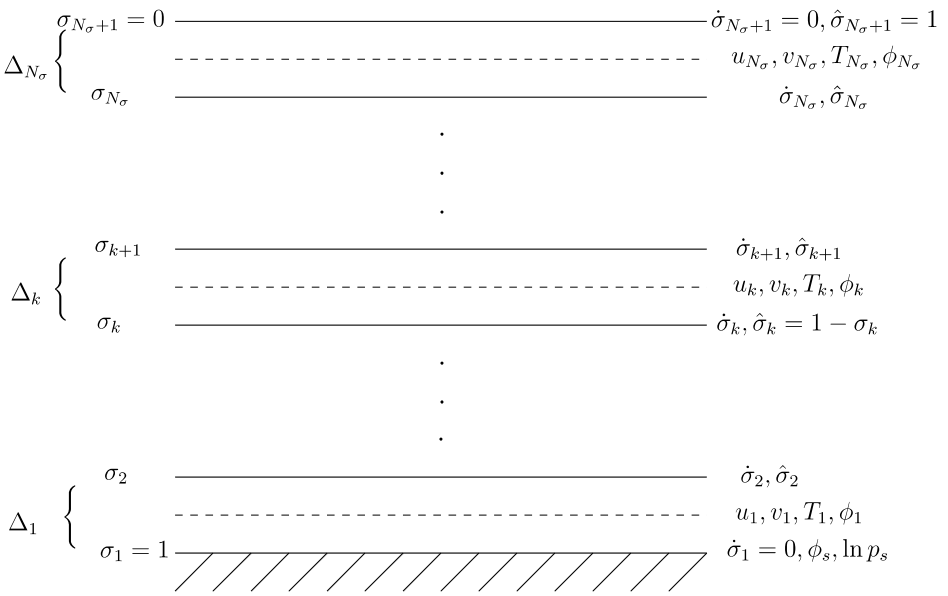

Fig. 1. Vertical distribution of model variables.

$$\sum_{k=1}^{N_\sigma} \Phi_k \Delta_k = \Phi_s + R \sum_{k=1}^{N_\sigma} T_k \Delta_k. \tag{20}$$

The hydrostatic equation is also written in the equivalent form

$$\frac{\partial \Phi}{\partial \sigma} + c_p \Theta \frac{\partial \Pi}{\partial \sigma} = 0 \tag{21}$$

where $\Pi = (p/p_0)^\kappa$ is the normalized pressure (p_0 is constant) and the virtual temperature Θ obeys the relation $T = \Pi\Theta$. We discretize (21) at layer interfaces as

$$\Phi_{k-1} - \Phi_k = \frac{c_p}{2}(\Theta_k + \Theta_{k-1})(\Pi_k - \Pi_{k-1}), \quad k = 2, \ldots, N_\sigma \tag{22}$$

and obtain:

$$\Phi_{k-1} - \Phi_k = c_p(T_{k-1} h_1(k-1) + T_k h_2(k-1)), \quad k = 2, \ldots, N_\sigma. \tag{23}$$

We have introduced the notation

$$h_1(k-1) = \frac{1}{2}\left(\frac{\Pi_k}{\Pi_{k-1}} - 1\right), \quad h_2(k-1) = \frac{1}{2}\left(1 - \frac{\Pi_{k-1}}{\Pi_k}\right), \quad k = 2, \ldots, N_\sigma \tag{24}$$

and observe that the ratios between values of Π on two consecutive vertical levels depend only on the values of σ on those levels, with $\Pi_k/\Pi_{k-1} = (\sigma_k/\sigma_{k-1})^\kappa$. Eqs. (20) and (23) establish the vertical relationship between temperature and geopotential, at any point on the Earth's surface:

$$\mathbf{C}\Phi = c_p \mathbf{H} T + \tilde{\Phi}_s \tag{25}$$

with the $N_\sigma \times N_\sigma$ matrices

$$\mathbf{C} = \begin{pmatrix} 1 & -1 & 0 & \cdots & 0 & 0 \\ 0 & 1 & -1 & \cdots & 0 & 0 \\ \cdot & \cdot & \cdot & \cdots & \cdot & \cdot \\ 0 & 0 & 0 & \cdots & 1 & -1 \\ \Delta_1 & \Delta_2 & \Delta_3 & \cdots & \Delta_{N_\sigma - 1} & \Delta_{N_\sigma} \end{pmatrix}$$

and

$$\mathbf{H} = \begin{pmatrix} h_1(1) & h_2(1) & 0 & \cdots & 0 & 0 \\ 0 & h_1(2) & h_2(2) & \cdots & 0 & 0 \\ \cdot & \cdot & \cdot & \cdots & \cdot & \cdot \\ 0 & 0 & 0 & \cdots & h_1(N_\sigma - 1) & h_2(N_\sigma - 1) \\ \kappa\Delta_1 & \kappa\Delta_2 & \kappa\Delta_3 & \cdots & \kappa\Delta_{N_\sigma - 1} & \kappa\Delta_{N_\sigma} \end{pmatrix}.$$

The vector $\tilde{\Phi}_s$ is given by $\tilde{\Phi}_s^t = (0, \ldots, 0, \Phi_s)$. Here and in the subsequent description we look at the three-dimensional fields (e.g. u, v, Φ and T) as vectors of two-dimensional fields, one at each of the N_σ layers and denote, for instance $T^t = (T_1, T_2, \ldots, T_{N_\sigma})$. We define $\mathbf{A} = c_p \mathbf{C}^{-1}\mathbf{H}$, where

$$\mathbf{C}^{-1} = \begin{pmatrix} 1 - \hat{\sigma}_2 & 1 - \hat{\sigma}_3 & 1 - \hat{\sigma}_4 & \cdots & 1 - \hat{\sigma}_{N_\sigma} & 1 \\ -\hat{\sigma}_2 & 1 - \hat{\sigma}_3 & 1 - \hat{\sigma}_4 & \cdots & 1 - \hat{\sigma}_{N_\sigma} & 1 \\ \cdot & \cdot & \cdot & \cdots & \cdot & \cdot \\ -\hat{\sigma}_2 & -\hat{\sigma}_3 & -\hat{\sigma}_4 & \cdots & 1 - \hat{\sigma}_{N_\sigma} & 1 \\ -\hat{\sigma}_2 & -\hat{\sigma}_3 & -\hat{\sigma}_4 & \cdots & -\hat{\sigma}_{N_\sigma} & 1 \end{pmatrix}$$

(remembering that $\hat{\sigma}_i = \sum_{j=1}^{i-1} \Delta_j$), and get

$$\Phi = \mathbf{A}T + \bar{\Phi}_s^{3d}, \tag{26}$$

where we have introduced the notation $(\bar{\Phi}_s^{3d})^t = (\Phi_s, \Phi_s, \ldots, \Phi_s)$ for the replication of a surface field to all σ-levels.

We provide now the details about the thermodynamic equation (13). There are two terms in the RHS of this equation treated implicitly, one of which is $-\kappa T_0 \int_0^1 D\,\mathrm{d}\sigma$, discretized in the vertical as $-\kappa T_0 \sum_{k=1}^{N_\sigma} \Delta_k D_k$. The other term is the part of the term $\kappa T_0 \dot{\sigma}/\sigma$ which is handled implicitly. The vertical discretization of this quantity begins by rewriting it as

$$\kappa T_0 \frac{\dot{\sigma}}{\sigma} = \frac{T_0}{\Pi} \dot{\sigma} \frac{\partial \Pi}{\partial \sigma} = \frac{T_0}{\Pi} \left(\frac{\partial (\dot{\sigma} \Pi)}{\partial \sigma} - \Pi \frac{\partial \dot{\sigma}}{\partial \sigma} \right). \tag{27}$$

From this expression we derive the discrete form:

$$\frac{T_0}{\Pi_k} \left(\frac{\dot{\sigma}_k \tilde{\Pi}_k - \dot{\sigma}_{k+1} \tilde{\Pi}_{k+1}}{\Delta_k} - \Pi_k \frac{\dot{\sigma}_k - \dot{\sigma}_{k+1}}{\Delta_k} \right), \tag{28}$$

where $\dot{\sigma}_k$ is defined at the interface between layers k and $k-1$ and $\tilde{\Pi}_k$, at the same interface, is defined as $\tilde{\Pi}_k = (\Pi_k + \Pi_{k-1})/2$. Using this definition in (28) we get the discretization:

$$\kappa T_0 \frac{\dot{\sigma}}{\sigma} \approx -\frac{T_0}{2\Delta_k} \left(\dot{\sigma}_{k+1} \left(\frac{\Pi_{k+1}}{\Pi_k} - 1 \right) + \dot{\sigma}_k \left(1 - \frac{\Pi_{k-1}}{\Pi_k} \right) \right). \tag{29}$$

We now use (12) for deriving the discrete form

$$\dot{\sigma}_k = \sum_{j=1}^{k-1} \Delta_j (\mathbf{V_j} \cdot \nabla_H \ln p_s + D_j) - \hat{\sigma}_k \sum_{j=1}^{N_\sigma} \Delta_j (\mathbf{V_j} \cdot \nabla_H \ln p_s + D_j) \tag{30}$$

(remember that $\hat{\sigma} = 1 - \sigma$ and that the vertical indexing follows this variable as in Fig. 1). Now, recalling that only the sums involving the wind divergence in the definition of $\dot{\sigma}_k$ belong to the implicit term of the thermodynamic equation (13), and using (29), (24) and (30) we get the expression for the discrete form of this implicit term:

$$\frac{T_0}{\Delta_k} \left[h_1(k) \left(\hat{\sigma}_{k+1} \sum_{j=1}^{N_\sigma} \Delta_j D_j - \sum_{j=1}^{k} \Delta_j D_j \right) + h_2(k-1) \left(\hat{\sigma}_k \sum_{j=1}^{N_\sigma} \Delta_j D_j - \sum_{j=1}^{k-1} \Delta_j D_j \right) \right], \quad k = 1, \ldots, N_\sigma$$

with $h_2(0) = h_1(N_\sigma) = 0$. The discrete thermodynamic equation can then be put together as

$$T^{n+1} + \Delta t \mathbf{B} D^{n+1} = R_T, \tag{31}$$

where the right-hand side R_T depends on variables at previous time steps and the $N_\sigma \times N_\sigma$ matrix $\mathbf{B}$ couples the equations on the different vertical layers. This matrix can be written as

$$\mathbf{B} = T_0 \mathbf{M}^{-1} \mathbf{H}^t (\mathbf{C}^{-1})^t \mathbf{M} \tag{32}$$

with the matrices $\mathbf{H}$ and $\mathbf{C}$ as before. We have introduced the diagonal matrix $\mathbf{M}$ whose diagonal terms are defined as $\mathbf{M}_{i,i} = \Delta_i, i = 1, \ldots, N_\sigma$. After the temporal and vertical discretization we obtain from Eqs. (10), (31) and (18) the implicit system to be solved:

$$\begin{aligned} & J \begin{bmatrix} u^{n+1} \\ v^{n+1} \end{bmatrix} + \Delta t \nabla_H P^{n+1} = \begin{bmatrix} R_u \\ R_v \end{bmatrix}, \\ & T^{n+1} + \Delta t \mathbf{B} D^{n+1} = R_T, \\ & l'^{n+1} + \Delta t R T_0 \delta .\, D^{n+1} = R_l, \end{aligned} \tag{33}$$

where

$$J = \begin{bmatrix} 1 & -F \\ F & 1 \end{bmatrix}, \quad F = \Delta t f, \quad R_{\mathbf{V}} = \begin{bmatrix} R_u \\ R_v \end{bmatrix} \quad \text{and} \quad \delta^t = (\Delta_1, \ldots, \Delta_{N_\sigma}).$$

From Eqs. (17) and (26) we get

$$P = \mathbf{A}T + (RT_0)\ \bar{l}'^{3d} \tag{34}$$

with $(\bar{l}'^{3d})^t = (l', l', \ldots, l')$. Combining Eq. (34) with (33) we obtain

$$P^{n+1} = -\Delta t(\mathbf{AB}D^{n+1} + (RT_0)^2\mathbf{NM}D^{n+1}) + \mathbf{A}R_T + (RT_0)\ \bar{R}_l{}^{3d}, \tag{35}$$

which we will denote by

$$P^{n+1} = -\Delta t\mathbf{E}D^{n+1} + R_{\mathrm{P}}. \tag{36}$$

The matrix $\mathbf{N}$ introduced in (35) has all entries equal to 1. After multiplying the momentum equation in (33) by

$$J^{-1} = \begin{bmatrix} G & FG \\ -FG & G \end{bmatrix} \tag{37}$$

(where $G = 1/(1+F^2)$), we take its horizontal divergence in order to get

$$D^{n+1} = -\Delta t\nabla_{\mathrm{H}} \cdot (J^{-1}\nabla_{\mathrm{H}}P^{n+1}) + \nabla_{\mathrm{H}} \cdot J^{-1}R_{\mathbf{V}}. \tag{38}$$

Substitution of this equation into (36) leads to a three-dimensional (elliptic) scalar equation for the generalized geopotential

$$P^{n+1} - \Delta t^2\mathbf{E}\nabla_{\mathrm{H}} \cdot (J^{-1}\nabla_{\mathrm{H}}P^{n+1}) = R_{\mathrm{P}} - \Delta t\mathbf{E}\nabla_{\mathrm{H}} \cdot J^{-1}R_{\mathbf{V}}. \tag{39}$$

The vertical coupling matrix $\mathbf{E}$ gives the character of this equation. We now prove:

Proposition 1. *The vertical structure matrix* $\mathbf{E}$ *has a complete set of eigenvectors and real positive eigenvalues.*

Proof 1. The vertical structure matrix is given by $\mathbf{E} = \mathbf{AB} + (RT_0)^2\mathbf{NM}$. Using the expressions for $\mathbf{A}$ and $\mathbf{B}$ we get

$$\begin{aligned}\mathbf{E} &= c_{\mathrm{p}}T_0\mathbf{C}^{-1}\mathbf{H}\mathbf{M}^{-1}\mathbf{H}^t(\mathbf{C}^{-1})^t\mathbf{M} + (RT_0)^2\mathbf{NM} = c_{\mathrm{p}}T_0(\mathbf{C}^{-\mathbf{1}}\mathbf{H}\mathbf{M}^{-1}\mathbf{H}^t(\mathbf{C}^{-1})^t + \kappa RT_0\mathbf{N})\mathbf{M} \\ &= c_{\mathrm{p}}T_0(\mathbf{C}^{-1}\mathbf{H}\mathbf{M}^{-1/2}(\mathbf{M}^{-1/2})^t\mathbf{H}^{\mathbf{t}}(\mathbf{C}^{-1})^t + \kappa RT_0\mathbf{N})\mathbf{M}.\end{aligned}$$

It follows that multiplying $\mathbf{E}$ on the right by $\mathbf{M}^{-1}$ leads to

$$\mathbf{E}\mathbf{M}^{-1} = c_{\mathrm{p}}T_0(\mathbf{S}\mathbf{S}^t + \kappa RT_0\mathbf{N})$$

with $\mathbf{S} = \mathbf{C}^{-1}\mathbf{H}\mathbf{M}^{-1/2}$. Notice that

$$x.\mathbf{N}x = \left(\sum_{i=1}^{N_\sigma} x_i\right)^2$$

for every $x \in R^{N_\sigma}$. We then have that $\mathbf{N}$ is symmetric positive semi-definite and therefore the matrix $\mathbf{E}\mathbf{M}^{-1}$ is symmetric positive definite. And so is the matrix $\mathbf{T} = \mathbf{M}^{1/2}(\mathbf{E}\mathbf{M}^{-1})\mathbf{M}^{1/2}$, having therefore a complete set of eigenvectors and positive eigenvalues. Notice that $\mathbf{T} = \mathbf{M}^{1/2}\mathbf{E}\mathbf{M}^{-1/2}$, showing that $\mathbf{T}$ and $\mathbf{E}$ are similar and share the same eigenvalues. Now let $\mathbf{U}$ be an orthogonal matrix diagonalizing $\mathbf{T}$. We then have $\mathbf{\Lambda} = \mathbf{U}^t\mathbf{T}\mathbf{U} = \mathbf{U}^t\mathbf{M}^{1/2}\ \mathbf{E}\mathbf{M}^{-1/2}\mathbf{U}$, with $\mathbf{\Lambda}$ diagonal, with the eigenvalues of $\mathbf{T}$ in the diagonal. Therefore, $\mathbf{E}\mathbf{M}^{-1/2}\mathbf{U} = \mathbf{M}^{-1/2}\mathbf{U}\mathbf{\Lambda}$. This shows that the columns of the matrix $\mathbf{L} = \mathbf{M}^{-1/2}\mathbf{U}$ build a basis of eigenvectors of $\mathbf{E}$, completing the proof. □

We can now multiply Eq. (39) by $\mathbf{L}^{-1}$ (where $\mathbf{L}$ is the matrix of the eigenvectors of $\mathbf{E}$) in order to get:

$$\widehat{P}^{n+1} - \Delta t^2\mathbf{\Lambda}\nabla_{\mathrm{H}} \cdot (J^{-1}\nabla_{\mathrm{H}}\widehat{P}^{n+1}) = \mathbf{L}^{-1}(R_{\mathrm{P}} - \Delta t\mathbf{E}\nabla_{\mathrm{H}} \cdot J^{-1}R_{\mathbf{V}}), \tag{40}$$

where $\widehat{P} = \mathbf{L}^{-1}P$ (observe that the vertical operator $\mathbf{L}^{-1}$ and the horizontal differential operators commute). The multiplication by $\mathbf{L}^{-1}$ decouples the three-dimensional equation into a set of N_σ independent two-dimensional Helmholtz-type equations, which are elliptic since the eigenvalues of $\mathbf{E}$ are positive. After solution of this set of equations, the generalized geopotential is obtained by forming $P^{n+1} = \mathbf{L}\widehat{P}^{n+1}$ and used to determine the wind field and divergence, from which the temperature and the logarithm of the surface pressure can be derived according to (33).

We observe that other authors employ a similar treatment, but based on the assumption of the existence of a basis of eigenvectors and positive eigenvalues as e.g. in [6].

2.3. Spatial discretization

The method described so far could be used in conjunction with different approaches to the spatial discretization. One could adopt finite-elements, finite-differences or even spectral developments to discretize the fields on each σ-layer. We employ second order finite-differences on a uniform (λ, θ) latitude/longitude Arakawa C-grid (cf. Fig. 2), with mesh-sizes $\Delta_\lambda = \Delta_\theta = \pi/N_\theta$, where $N_\theta + 1$ is the number of grid-latitudes (including the poles) and $N_\lambda = 2N_\theta$ is the number of longitudes, on each layer. With a C-grid distribution, we have the model variables on convenient locations for centered differences. For instance, short (one mesh-size) differences can be employed when discretizing the gradient of the generalized geopotential. The same is true in the computation of the horizontal divergence. However, some terms of the equations require average of the wind components, when those are required at the locations of the other variables. This is the case for the Coriolis terms and also for the evaluation of $V \cdot \nabla_H \ln p_s$ in the thermodynamic equation.

The momentum equation has been written and discretized in vector form. When equating terms at the arrival and departure points we have to consider that at each point on the sphere the local coordinate system changes. To compare the vector components at two different locations we need to represent them at the same system of reference. For doing this we adopt as reference the tangent plane at the middle of the trajectory, with unitary coordinates in the local λ and θ direction. This approach is described in detail by Ritchie in [15] and we follow it closely. In component form, in spherical coordinates, the equations have the form

$$u^{n+1} - \Delta t f v^{n+1} + \frac{\Delta t}{2a\cos\theta}\frac{\partial P^{n+1}}{\partial \lambda} = r_u, \tag{41}$$

$$v^{n+1} + \Delta t f u^{n+1} + \frac{\Delta t}{2a}\frac{\partial P^{n+1}}{\partial \theta} = r_v. \tag{42}$$

They are combined to form the divergence at time t_{n+1}, according to Eq. (38). We keep the analytic form of the operators involved in the left-hand side of the equations until forming the equation for the generalized geopotential (39), which leads to the Helmholtz-type equations (40) associated with each of the eigenvalues λ_k of matrix **E**. In spherical coordinates these equations have the form

$$\mu_k \widehat{P} - \frac{G}{\cos^2\theta}\frac{\partial^2 \widehat{P}}{\partial \lambda^2} + \frac{1}{\cos\theta}\left(\frac{\partial FG}{\partial \theta}\frac{\partial \widehat{P}}{\partial \lambda} - \frac{\partial}{\partial \theta}\left(G\cos\theta\frac{\partial \widehat{P}}{\partial \theta}\right)\right) = r_{\mathrm{p}} \tag{43}$$

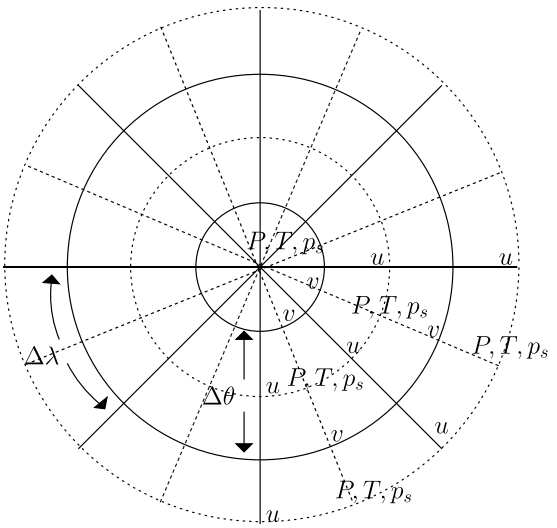

Fig. 2. C-grid and model variables close to the pole.

with $\mu_k = a^2/(\lambda_k \Delta t^2)$, a being the Earth's radius. Only at this point we discretize the differential operator through centered differences. We point out, however, that the right-hand sides r_u and r_v (from (41) and (42)) are discretized on the C-grid. The application of the inverse J^{-1} (37) at the corresponding grid locations requires interpolation of r_u to v-locations and of r_v to u-points. The resulting quantities are then properly located for the application of the discrete divergence operator, and the right-hand side of (38) is completed. We notice that similar approaches have been used in [5,6], leading to Helmholtz-type equations of the same form.

The formal singularity at the poles in (43) can be removed by switching to an integral form and use of quadrature rules (compare [4] for details). As in [5,4] we employ a multigrid scheme (based on [2]) in order to solve the equations. We point out that for the larger eigenvalues of **E**, the contribution of the term μ_k is very small and the behaviour of the multigrid method will be similar to the case of a Poisson equation. For the smaller eigenvalues, the discrete matrix becomes more diagonally dominant and the convergence rates are even improved.

The Helmholtz-type equation on the sphere, discretized by finite-differences on a uniform latitude–longitude grid, leads to a highly anisotropic operator close to the poles. As a consequence, usual point relaxation methods such as red–black or lexicographical Gauss-Seidel provide poor smoothing of the errors. The use of line-relaxation, where the unknowns at the same latitude are updated simultaneously (through the solution of a periodical tridiagonal system at each latitude), provides appropriate smoothing for an efficient method (cf. [2]). The other components of the multigrid solver are bilinear interpolation of the coarse grid correction and full-weighting restriction of residuals. A $\mathbf{V}(1,1)$ cycle (with one sweep of relaxation before and one after the coarse grid correction) guarantees convergence factors below 0.1 (this means that each multigrid cycle reduces the error by a factor larger than 10). We employ a full-multigrid scheme, where solutions on coarser grids (after bicubic interpolation) are used as initial approximations on finer grids (see [2]). In the section on numerical results we will see the effects of the different eigenvalues defining the parameter μ_k on the behaviour of the multigrid scheme.

2.4. Summary of a time-step

We summarize now all the stages required for a time-step. Given the model fields on the computational grid on two consecutive times t_{n-1} and t_n, the determination of the new fields at time t_{n+1} comprises:

- Evaluation of the vertical velocity $\dot{\sigma}(t_n)$ at every grid-point according to the discrete form of Eq. (12).
- Computation of the departure points at every grid-point through the iterative process (8) and (9). Details about the spherical geometry are handled as in [14]. Due to the use of a C-grid, we need different trajectories related to the P, u and v grid-points. We compute the trajectories having the P grid-points as arrival points and obtain the other two through linear interpolation.
- Computation of the vertically averaged mean horizontal wind and of the corresponding two-dimensional departure points (as in iteration (8), but with a wind field independent of σ).
- Evaluation on the computational grid of the terms that will build the right-hand sides of Eqs. (10), (13) and (18). The explicit terms are computed at time t_n and the ones which are treated implicitly at time t_{n-1}. The necessary interpolations to departure points are carried out.
- Right-hand sides of the momentum equations are transformed to have the equations in component form (details are as in [15]).
- Computation of the right-hand side for Eq. (39), followed by the multiplication by the precomputed inverse of matrix **L**, formed by the eigenvectors of **E**.
- Multigrid solution of the N_σ resulting Helmholtz-type Eq. (43), associated with the eigenvalues of **E**.
- The solutions of Eq. (43) are multiplied by **L** to obtain the generalized geopotential P.
- Computation of the horizontal gradient of P and determination of the horizontal wind field **V** through (41) and (42).
- Computation of the new horizontal divergence and determination of T^{n+1} and l^{n+1} using (33).

We observe that matrix **E** is time and spatial location independent. It is precomputed, as well its eigenvectors and eigenvalues (matrices **L** and $\mathbf{\Lambda}$). Since we are dealing with a three-time-level method, the first time-

step requires a special treatment. We employ a slow start k-step procedure, in which we define $\delta_t = \Delta t/2^k$. We initially assume that the fields at time $t_0 + \delta_t$ are the same as the initial values at t_0. Performing one time-step with time increment equal to δ_t we get an approximation for the fields at $t = t_0 + 2\delta t$. We now double δ_t and repeat the time-step, using the values at t_0 and $t_0 + \Delta t/2^{k-1}$ to get an approximation at time $t_0 + \Delta t/2^{k-2}$. We repeat this process, doubling δ_t at each step till we get an approximation at time $t_0 + \Delta t$. From there on we proceed normally with Δt time increments. We normally take $k = 2$ in our numerical experiments. Another observation related to the use of a three-time-level method is that this type of discretization has a computational mode slightly unstable. In order to prevent its growth we employ a Robert/Asselin type filter (with parameter 0.025) (cf. [1]).

3. Numerical results

In this section, we provide several results concerning the performance and quality of the results obtained with our model. We begin with results obtained for a model test case, proposed by Polvani et al. [13].

3.1. Model validation

One of the problems concerning the validation of models for the primitive equations is the fact that analytic solutions are not available. Recently, a new test case has been suggested, for which the authors were able to compute converged numerical solutions with two different numerical models [13]. The test consists of a 12-day integration of the unforced primitive equations from a prescribed initial state (a baroclinically unstable mid-latitude jet), whose details are provided in [13]. There is, however, one modification to the equations, which is the explicit inclusion of a diffusion term in the thermodynamic and momentum equations (necessary to prevent the development of finite-time singularities, according to the authors). The Laplacian of the respective variables (T, u and v) multiplied by a diffusion coefficient is added to the right-hand side of the equations.

We have added in our numerical scheme an implicit discretization of the diffusion term, through a fractional step method, as done in spectral models (for instance, in [17]). A time-step is carried out as before but the new values of the fields are seen as provisional values, which will be altered by the diffusion step in the following manner: for instance, if $\tilde{T}^{n+1}$ is the temporary value of the new temperature, we compute the new temperature by solving the equation

$$T^{n+1} - 2\nu\Delta t\nabla^2 T^{n+1} = \tilde{T}^{n+1},$$

where $\nu = 7 \times 10^5$ m^2/s is the diffusion coefficient. This leads to the necessity of solving a two-dimensional Helmholtz equation on each model layer, for each of the three variables involved, at the end of every time-step. We again employ a multigrid method in the solution of these equations.

We now show the results that we have obtained with different model resolutions, providing evidence of the convergence of the solutions with the refinements of the meshes. In Fig. 3 we display the time evolution of the temperature field in the northern hemisphere (from latitude 15 to 85), where the instabilities develop. These results were computed on a 256×128 lon/lat grid with 20 vertical layers (the temperatures shown in Fig. 3 are in the lowest layer of the model). We can see good agreement of these results with Fig. 2 of Polvani et al.'s article (the resolution of the latter is better, since a spectral T341L20 has been employed [13]).

In Fig. 4 we have the temperature field in the northern hemisphere after 12 days, obtained with different model resolutions. From top to bottom we employed a 128×64 grid with 20 layers, a 256×128 grid with 20 layers, a 256×128 grid with 40 layers and a 512×256 grid with 20 layers. The time-steps used were, respectively, 2400, 1200, 1200 and 600 s. We can observe good convergence of the results. We point out that we have also included results obtained with 40 model layers (third graphic from the top). In this case, $\sigma = 0.975$ is not in the middle of a model layer and the results were linearly interpolated from the two surrounding layers.

We now compare the computed vorticity field after 12 days of integration with several different resolutions. We point out that vorticity is not a prognostic variable in our model, but it is derived from the velocity fields, in contrast to Polvani's results obtained with spectral (and spectral element) schemes, which compute vorticity as a prognostic variable. In Fig. 5 we plot the vorticity field at the $\sigma = 0.975$ surface, for six different resolutions (details are given in the figure caption). We can observe that the results with a 128×64 grid (first two

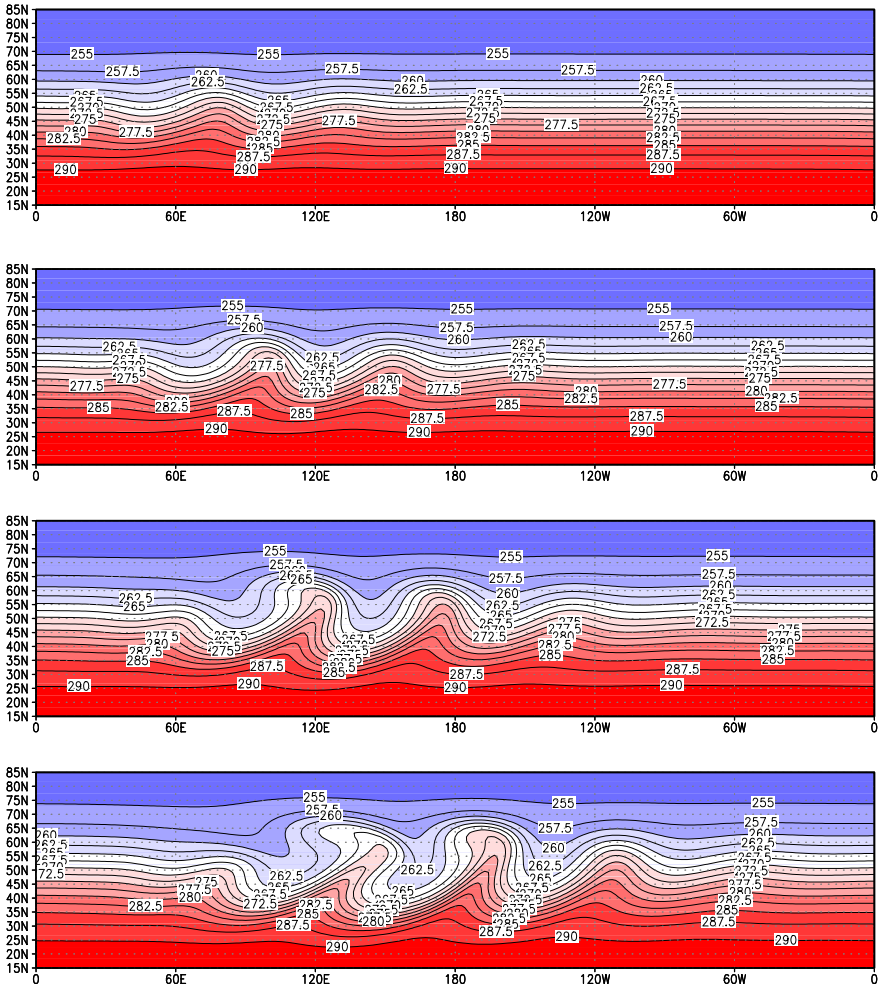

Fig. 3. Time evolution of the temperature field at layer $\sigma = 0.975$. From top to bottom we have the field after 6, 8, 10 and 12 days of integration. Computations used a 256×128 lon/lat grid with 20 vertical layers and time-steps of 600 s. The countour interval is 2.5 K and the temperature values lie between 252.5 K and 292.5 K.

graphics on top) are not converged, and the improvement brought by halving the time-step to 1200 s (in the second graphic). Further improvements towards convergence are gained by using a finer 256×128 grid (third graphic from the top) and then further halving the time-step (to 600 s, in the fourth graphic). In the fifth graphic we observe the effect of doubling the number of model layers to 40, while still keeping the 1200 s time step of the third graphic. Finally, in the bottom graphic we have the results with a 512×256 grid with 20 layers and a time-step of 600 s. The vorticity field has almost converged. The results are in good agreement with Polvani's results [13]. The patterns are pratically the same, although a bit less intense in some of the centers. The calculated maximum norm of the vorticity field at 256×128 and 512×256 grid resolution is of $7.7 \times 10^{-5}\ \mathrm{s}^{-1}$ (after 12 days, at the $\sigma = 0.975$ layer). The value obtained by Polvani et al. is $7.4 \times 10^{-5}\ \mathrm{s}^{-1}$.

In order to quantify the order of convergence we have computed L2-norms of the error at several resolutions with respect to a fine-grid reference solution (computed on a 512×256 mesh with 20 vertical layers and a time step of 300 s) for 12 days. In Figs. 6 and 7 we present the results at the lowest layer ($\sigma = 0.975$). We can observe that refining the mesh by a factor 4 reduces the error in Temperature after 12 days approximately by a factor of 16, presenting evidence of second order convergence. Very similar reduction factors are obtained for the wind variables u and v (not shown in the Figure). For the vorticity, which is not a primary model variable, the error reduction is slower. The error diminishes by a factor about 9 when we refine the mesh by a factor 4.

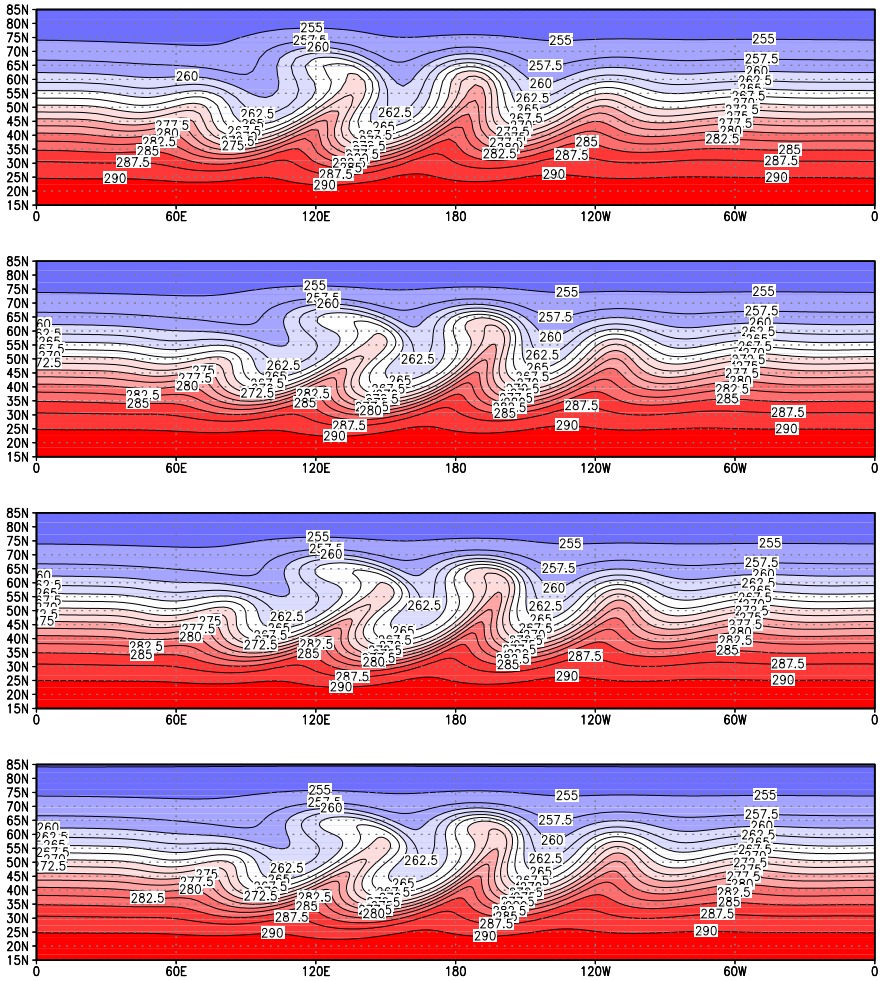

Fig. 4. Temperature field at layer $\sigma = 0.975$ after 12 days of integration, with different resolutions. From top to bottom we have: (a) $128 \times 64 \times 20$ grid, $\Delta t = 2400$ s, (b) $256 \times 128 \times 20$ grid, $\Delta t = 1200$ s, (c) $256 \times 128 \times 40$ grid, $\Delta t = 1200$ s and (d) $512 \times 256 \times 20$ grid, $\Delta t = 600$ s. Countour intervals are as in Fig. 3.

3.2. Multigrid performance

In this section, we consider the multigrid solution of the elliptic equations resulting from the semi-implicit discretization. We present results concerning the multigrid convergence factors and its variation with the diagonal term in the Helmholtz equations. Table 1 contains convergence factors of $\mathbf{V}(1,1)$-cycles for different resolutions and different eigenvalues λ_k (we take the six largest eigenvalues, convergence gets faster and faster for the smallest ones). The convergence factors are computed as the geometric mean residual reduction factor in the first 5 cycles (meaning that if v is this factor and R_0 the initial residual then after 5 cycles the residual will be $R_5 = v^5 R_0$). We observe that all factors are well below 0.1, with a typical multigrid efficiency for Poisson-type equations. We also notice that for the smaller eigenvalues the performance is even better, due to the increase in the diagonal dominance of the discrete operator. This effect is reduced for finer grids, although we get convergence to machine precision with only 2 or 3 cycles for the smallest eigenvalues, even with these fine-grids.

With the achieved convergence factors and the use of the Full-Multigrid algorithm, just a few cycles will be sufficient to solve the equations to machine precision. In practice this is not necessary and two multigrid cycles provide good accuracy.

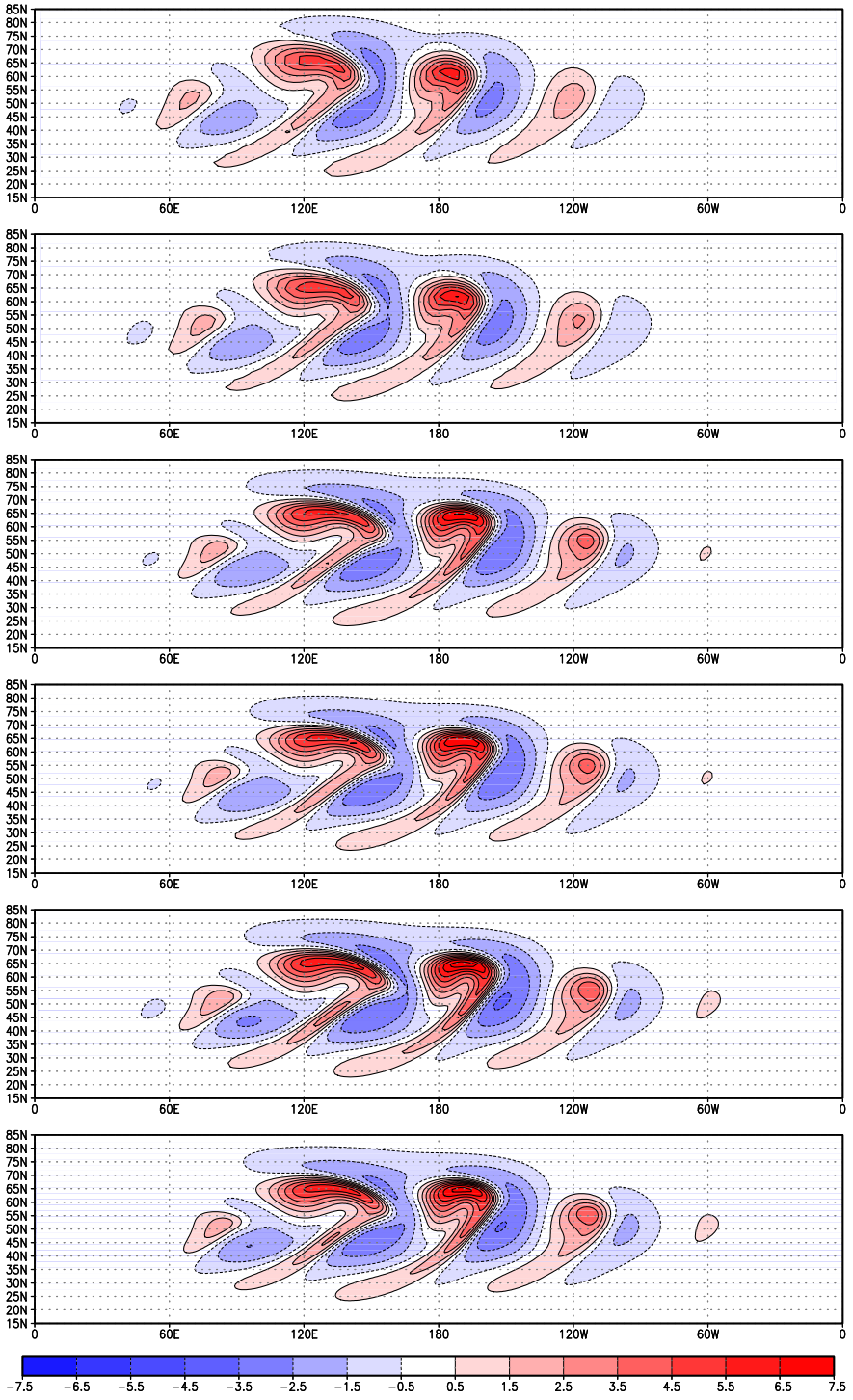

Fig. 5. Vorticity field at layer $\sigma = 0.975$ after 12 days of integration, with different resolutions. From top to bottom we have: (a) $128 \times 64 \times 20$ grid, $\Delta t = 2400$ s, (b) $128 \times 64 \times 20$ grid, $\Delta t = 1200$ s, (c) $256 \times 128 \times 20$ grid, $\Delta t = 1200$ s, (d) $256 \times 128 \times 20$ grid, $\Delta t = 600$ s, (e) $256 \times 128 \times 40$ grid, $\Delta t = 1200s$ and (f) $512 \times 256 \times 20$ grid, $\Delta t = 600$ s. The range of contours varies from -7.5 to 7.5×10^{-5} s^{-1} with countour interval of 1×10^{-5} s^{-1}.

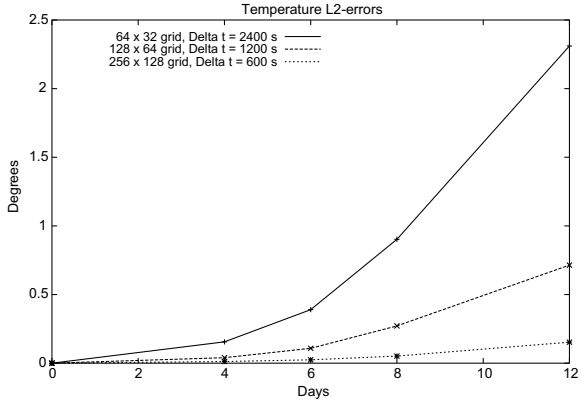

Fig. 6. Time evolution of Temperature L2 error norms at several resolutions. Errors are computed with respect to a fine-resolution reference run on a 512×256 grid with $\Delta t = 300$ s, at the layer $\sigma = 0.975$. All runs used 20 vertical layers.

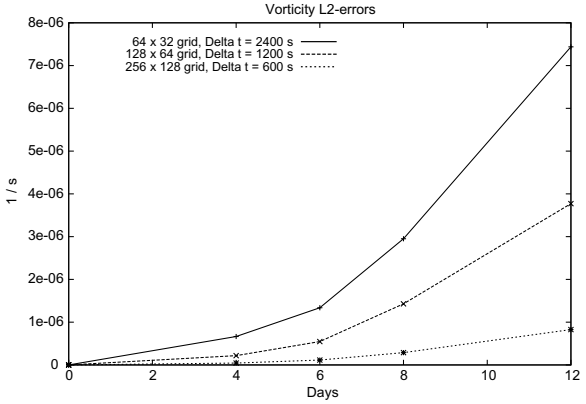

Fig. 7. As in Fig. 6 but for Vorticity L2 error norms.

Table 1
Multigrid convergence factors for Eq. (43) with the largest values of the eigenvalues λ_k

Horizontal grid	96×49	192×97	384×193
Largest eigenvalue	0.050	0.055	0.048
Second eigenvalue	0.036	0.054	0.052
Third eigenvalue	0.015	0.045	0.055
Fourth eigenvalue	0.0048	0.028	0.052
Fifth eigenvalue	0.0014	0.013	0.043
Sixth eigenvalue	0.0002	0.0063	0.032

Results are shown for different horizontal grid resolutions. In all cases we have used $\Delta t = 1h$ and 28 vertical layers.

3.3. Treatment of orography

We present some results concerning the comparison between two different model formulations. One uses $\ln p_s$ as the variable to be advected (according to Eq. (16)), as commonly chosen, for example in [16,6]. In our model formulation we considered the splitting (17) with the formulation (18) used for the advection of the surface pressure (a similar change has been used in [19]). In Fig. 8 we see model results for the temperature field at the fifth lowest model layer after 2 days of integration with $\Delta t = 1h$ in the South American region. We can see (bottom left) the noise generated close to the Andes, where we have a strong

3.4. Handling of the continuity equation

We propose in the present paper a new way of handling the continuity equation in semi-Lagrangian models, with the advection through the mean wind as in Eq. (15). Alternative formulations (as in [6]) use a projection of the three-dimensional Lagrangian trajectory on each layer, advect $\ln p_s$ on each layer according to these projected trajectories and integrate (average) the final result. Another approach (see [17]) uses the full three-dimensional Lagrangian trajectory, performs three-dimensional interpolation of the forcing terms and integrates (averages) at the end. The main advantage of our approach is that it is purely two-dimensional after computing the mean wind and therefore is simpler and computationally cheaper. We have implemented the three alternatives and the results are similar (see Fig. 9). We observe that using the averaged wind or the full three-dimensional wind leads practically to the same results (the RMS differences after 3 days amount to 0.5 m in the 500 hPa surface, shown in Fig. 9). After 5 days the RMS differences are of 0.8 m. On the 850 hPa surface we have differences of 0.5 m after 3 days and of 0.9 m after 5 days. Results obtained with the projected three-dimensional winds are also similar, but larger differences can be observed (1.9 m after 3 days and 3.3 m after 5 days at 500 hPa, and 2.1 and 3.5 m after, respectively, 3 and 5 days at 850 hPa). Larger RMS differences also result from the direct comparison between the results with the projected three-dimensional winds and with the full three-dimensional wind (1.6 and 2.8 m after, respectively, 3 and 5 days at 500 hPa and corresponding values of 1.7 and 3.1 m at 850 hPa).

None of these formulations will lead to a formally conservative semi-Lagrangian scheme. There is some debate about which of the formulations (as in [6] or in [17]) would present better conservation properties. We compared our approach with the other two on this matter and they have similar properties also regarding conservation, as shown in the 10 days integrations summarized in Fig. 10. The variations, of about 2–3 hPa in 10 days, are adequate for medium range forecasts. Again we notice that the projected winds lead to somewhat worse results.

We point out that the modification for treating steep orography also improves the conservation of the schemes. In [6] the authors employ a decentering parameter in their discretization, chosen in order to give a better conservation. We don't employ any decentering in our comparative results from Fig. 10. The modification for the orography is however used together with the three alternatives. We use in all other numerical experiments our 2D-approach, since it gives comparable results with less computational work.

3.5. Time-step variation

The great advantage of semi-Lagrangian over Eulerian models is the fact that they allow the use of much larger time-steps due to their improved stability properties. Using larger time-steps will make the model computationally more efficient. On the other hand, the choice of time-steps will be restricted by accuracy require-

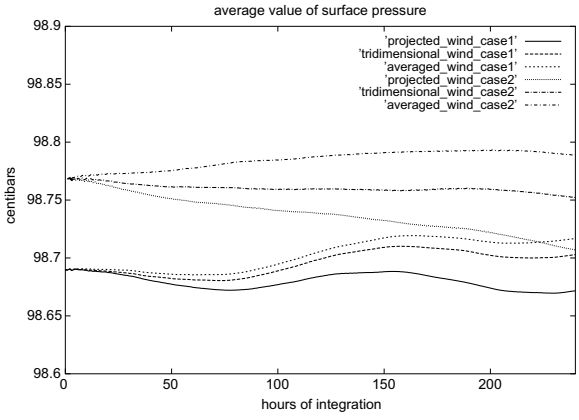

Fig. 10. Evolution of mean value of surface pressure for 10 days in two test cases (initial data from March 26th and May 19th 2004). The three different approaches for the continuity equation are compared. Integrations were on a 192×97 grid, 28 layers and $\Delta t = 60$ min.

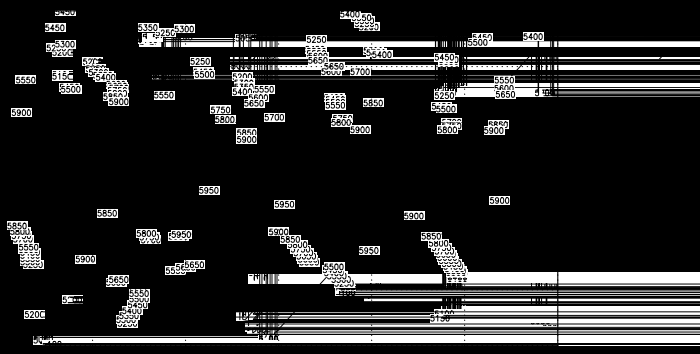

uniform resolution of 1.875° we compare for 5 days a reference run with a time-step of 20 min, with runs with 40 and 60 min time-steps. The same types of results are presented for the finer resolution of 0.9375° (384×197 grid). We point out that we have employed no initialization tailored for our model. The initial states have been initialized (with normal mode initialization) for CPTEC's Eulerian spectral model. We also interpolated the initial values to the C-grid locations, since the spectral model employs a gaussian grid. This explains why the error grows faster at the beginning of the integration (first 6 h), since the fast gravity waves which remain in the initial states won't be well resolved with time-steps above the CFL restriction. In spite of this, the error growths in relation to the reference run (of about 2–4 m a day) are small and the use of larger time-steps is acceptable in terms of accuracy.

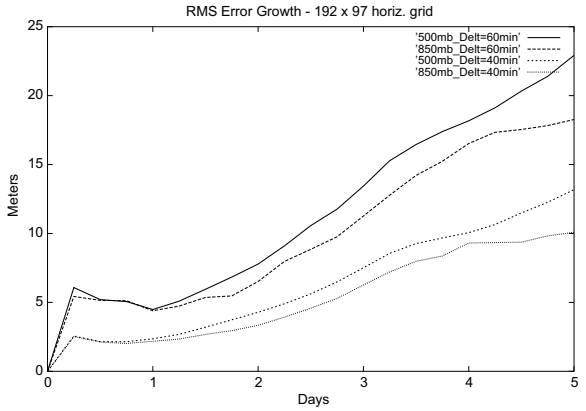

Fig. 13. Root mean square error growth in comparison to reference run with $\Delta t = 20$ min on a 192×97 grid with 28 vertical layers. Results employed $\Delta t = 40$ min and $\Delta t = 60$ min.

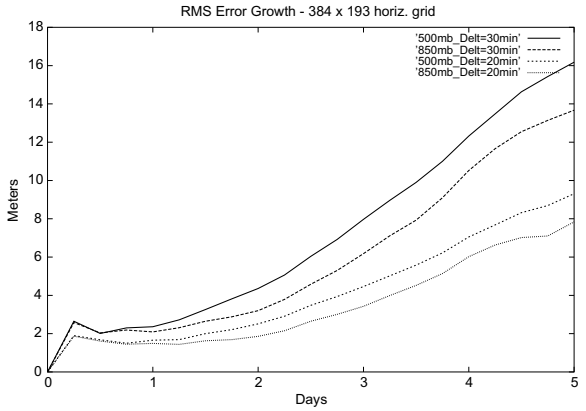

Fig. 14. Root mean square error growth in comparison to reference run with $\Delta t = 10$ min on a 384×193 grid with 28 vertical layers. Results employed $\Delta t = 20$ min and $\Delta t = 30$ min.

In [6] the authors use the fields after two days of integration with a decentering (dissipative) parameter as initial state. This initial integration acts as a dynamic initialization and helps to filter out the gravity waves of the initial state. We do not do this in our experiments and prefer to show the results as they are, with this initial error growth present. Anyway, the results show that time-steps three-times larger than CFL restrictions still furnish good accuracy and can be used in conjunction with the semi-Lagrangian model. The use of large time-steps with similar accuracy makes the Lagrangian scheme very efficient, comparing favorably to Eulerian models.

3.6. Model performance

Our model presents a computational complexity per time-step which is almost linear on the number of grid-points. An exception occurs when decoupling the three-dimensional elliptic Eq. (39) into a set of two-dimensional equations, since the matrix multiplication required is quadratic on the number of layers. In Table 2 we

Table 2
CPU-times (in s) for the execution of 100 time-steps of the model at different resolutions

Layers↓ Grid→	192×97	384×193
14	307.58	1226.05
28	668.96	2638.19

furnish computational times for the execution of 100 model time-steps at two different resolutions, first with 1.875° of resolution, both in latitudinal and longitudinal directions, and also with 0.9375° (corresponding to a horizontal grid of 384×193 grid-points). In both runs we employ 28 model layers. The grid has over 2 million grid-points in the finer resolution. All computational results with our model have been obtained on a PC (with a 3.2 GHz Pentium 4, 2 MB cache and 3 GB of memory). We also compare the times to run the model with 14 vertical layers and with 28 layers, seeing the effects of the quadratic complexity of the decoupling process. We can also observe that the cpu-times grow linearly with the grid-points when the number of layers is the same.

We see that the finite-difference model furnishes an attractive alternative in terms of computational efficiency for global integrations. A 10 days integration at the fine 384×193 mesh, with 28 model layers and time-steps of 30 min (with good accuracy as shown before) will require about 12,500 s, or about three and a half hours on a PC. Spectral models, although amenable to very efficient implementations on parallel and vector computers (eg. [3]), present the potential drawback of the higher computational complexity associated with Legendre transforms.

4. Conclusions

We have developed a semi-implicit semi-Lagrangian model for a finite-difference discretization of the global primitive equations. The model employs spherical coordinates combined with a σ-coordinate in the vertical direction. We introduced a new way of handling the continuity equation which is more efficient than other approaches, while providing similar numerical results. We have adopted a spatially averaged Eulerian way of handling orography (based on [18]), which has proven to contribute to better results with large time-steps in presence of steep orography. We have successfully employed a multigrid solver in the solution of the elliptic equations resulting from the semi-implicit method, after a vertical decoupling, which we prove to be feasible. We carried out several integrations with the test case proposed in [13] for the validation of the dynamical cores of primitive equation models. The results produced by our model are in general in good agreement with the converged results given in [13].

The global model has proven to be very stable, enabling the use of time-steps which by far exceed the corresponding CFL conditions related to Eulerian discretizations. We present numerical integrations with real weather data evidencing that we can triple the time-step used by Eulerian schemes, with acceptable accuracy. This makes the model very efficient. We can run a ten day simulation, with time-steps of half an hour, at a relatively fine resolution (0.9375° on the sphere, 28 vertical layers), in about three and a half hours on a personal computer.

The model we have presented in this paper gives us the basis for the development of a full model with variable resolution based on local refinements, extending our work done for shallow-water models in [4]. Other interesting further development would be the direct use of a multigrid scheme for the 3D-equation resulting from the semi-implicit discretization, which would reduce the computational complexity of this part of the model to linear. This is part of ongoing work.

Acknowledgements

We acknowledge financial support from CAPES (Prodoc – App. Math. USP) and Fapesp (01-13104-1, 01-07068-2). We thank the referees for the careful reading and useful comments.

References

[1] R. Asselin, Frequency filter for time integrations, Mon. Wea. Rev. 100 (1972) 487–490.
[2] S.R.M. Barros, Multigrid methods for two- and three-dimensional Poisson-type equations on the sphere, J. Comput. Phys. 92 (1991) 313–348.
[3] S.R.M. Barros, D. Dent, L. Isaksen, G. Robinson, G. Mozdzynski, F. Wollenweber, The IFS model: a parallel production weather code, Parallel Comput. 21 (1995) 1621–1638.
[4] S.R.M. Barros, C.I. Garcia, A global semi-implicit semi-Lagrangian shallow-water model on locally refined grids, Mon. Wea. Rev. 132 (2004) 53–65.

[5] J.R. Bates, F.H.M. Semazzi, R.W. Higgins, S.R.M. Barros, Integration of the shallow-water equations on the sphere using a vector semi-Lagrangian scheme with a multigrid solver, Mon. Wea. Rev. 118 (1990) 1615–1627.
[6] J.R. Bates, S. Moorthi, R.W. Higgins, A global multilevel atmospheric model using a vector semi-Lagrangian finite-difference scheme. Part I: adiabatic formulation, Mon. Wea. Rev. 121 (1993) 244–263.
[7] J. Côté, S. Gravel, A. Méthot, A. Patoine, M. Roch, A. Staniforth, The operational CMC-MRB global environmental multiscale (GEM) model. Part I: design considerations and formulation, Mon. Wea. Rev. 126 (1998) 1373–1395.
[8] M. Hortal, Aspects of the numerics of the ECMWF model, in Recent developments in numerical methods for atmospheric modelling, in: Proceedings of ECMWF Workshop, 1998, pp. 127–143.
[9] J.L. Kinter III, D. DeWitt, P.A. Dirmeyer, M.J. Fenessy, B.P. Kirtman, L. Marx, E.K. Schneider, J. Shukla, D.M. Strauss, The COLA atmosphere–biosphere general circulation model, volume 1: formulation, Report 51, Center for Ocean–Land–Atmosphere Studies, Maryland, USA, 1997.
[10] Y. Li, J. Ruge, J.R. Bates, A. Brandt, A proposed adiabatic formulation of three-dimensional global atmospheric models based on potential vorticity, Tellus 52A (2000) 129–139.
[11] K. Lindberg, V.A. Alexeev, A study of the spurious orographic resonance in semi-implicit semi-Lagrangian models, Mon. Wea. Rev. 128 (2000) 1982–1989.
[12] S. Moorthi, R.W. Higgins, J.R. Bates, A global multilevel atmospheric model using a vector semi-Lagrangian finite-difference scheme. Part II: version with physics, Mon. Wea. Rev. 123 (1995) 1523–1541.
[13] L.M. Polvani, R.K. Scott, S.J. Thomas, Numerically converged solutions of the global primitive equations for testing the dynamical core of atmospheric GCMs, Mon. Wea. Rev. 132 (2004) 2539–2552.
[14] H. Ritchie, Semi-lagrangian advection on a Gaussian grid, Mon. Wea. Rev. 115 (1987) 608–619.
[15] H. Ritchie, Application of the semi-Lagrangian method to a spectral model of the shallow-water equations, Mon. Wea. Rev. 116 (1988) 1587–1598.
[16] H. Ritchie, Application of the semi-Lagrangian method to a multilevel spectral primitive-equations model, Q. J. R. Meteorol. Soc. 117 (1991) 91–106.
[17] H. Ritchie, C. Temperton, A. Simmons, M. Hortal, T. Davies, D. Dent, M. Hamrud, Implementation of the semi-Lagrangian method in a high-resolution version of the ECMWF forecast model, Mon. Wea. Rev. 123 (1995) 489–514.
[18] H. Ritchie, M. Tanguay, A comparison of spatially averaged Eulerian and semi-Lagrangian treatments of mountains, Mon. Wea. Rev. 124 (1996) 167–181.
[19] C. Temperton, M. Hortal, A. Simmons, A two-time-level semi-Lagrangian global spectral model, Q. J. R. Meteorol. Soc. 127 (2001) 111–127.